In-situ Stereo-DIC with Thermal Imaging as a Process Monitoring Method in Vacuum-Assisted Thermoforming

Rasoul Varedi *, Bart Buffel, Frederik Desplentere *

Posted Date: 24 January 2024

doi: 10.20944/preprints202401.1733.v1

Keywords: Thermoforming; In-situ stereo DIC; Thermal camera synchronization; Forming step; Strain full field

Article

In-situ Stereo-DIC with Thermal Imaging as a Process Monitoring Method in Vacuum-Assisted Thermoforming

Rasoul Varedi [1,2,*], Bart Buffel [1,2] and Frederik Desplentere [1]

[1] Research Group ProPoliS, Department of Materials Engineering, KU Leuven Campus Bruges, Spoorwegstraat 12, 8200 Bruges, Belgium; Bart.Buffel@kuleuven.be, Frederik.Desplentere@kuleuven.be
[2] SIM M3 Program, Technologiepark 48, 9052 Zwijnaarde, Belgium
* Correspondence: Rasoul.Varedi@kuleuven.be

Abstract: This experimental study probes the dynamic behaviour of a 3mm ABS sheet during positive mould vacuum-assisted thermoforming. In this process, the sheet undergoes large and fast deformations, caused by the applied vacuum and mechanical stretching by the mould. The objective is to elucidate the complexities of these large, rapid and non-isothermal deformations. The non-isothermal conditions are caused by the radiative heating of the sheet, convective heat loss to the surrounding air and conductive heat transfer from the sheet to the mould. Utilizing stereo Digital Image Correlation (DIC) in tandem with thermal imaging, the present study accurately maps the occurring displacement, strain and strain rate field in relation to real-time temperature variation of the material. The study progresses to observe the ABS material from the moment it contacts the mould until it conforms to a positive 250mm diameter semi-sphere cast aluminium mould. The DIC methods are validated by comparing thickness values derived from DIC's principal strain directions to ultrasonic thickness gauge readings. This knowledge not only broadens the understanding of the thermo-mechanical behaviour of the material but also aids in optimizing process parameters for improved thickness uniformity in thermoformed products.

Keywords: thermoforming; in-situ stereo DIC; thermal camera synchronization; forming step; strain full field

1. Introduction

The vacuum assisted thermoforming process for heavy gauge thermoplastic sheets follows a sequential series of steps, beginning with the loading and clamping of a flat sheet. The material is then heated using a radiative heater bank, typically from both the top and bottom side of the sheet. This heating step brings the sheet to a soft, formable state. This heating phase is attentively controlled by setting a specific temperature, which is precisely measured using an infrared (IR) sensor. Despite the symmetrical arrangement of the heating elements aiming for uniform in plane heat distribution, the temperature across the sheet is almost inevitably uneven [1]. When a uniform heating pattern is applied, the center of the sheet often reaches a higher temperature compared to the clamped edges, resulting in a temperature gradient from the center to the edges [2]. Adjusting the in-plane temperature pattern of the sheet according to the mould shape is a method to enhance the quality of the thermoformed part [3]. During the heating process, the material also experiences thermal strain, leading to warpage. This warpage typically manifests as concave deformations both upward and downward which is caused by the material being constrained at its edges, thus hindering its ability to thermally expand freely [4]. In the pursuit of capturing intricate details of the mould shape, a common practice is to set a high temperature. However, the use of elevated temperature set points can induce sag deformation [5]. This occurs because of the lower stiffness of the material at high temperatures. The material loses its ability to support its own weight, resulting in sagging or off-

 doi:10.20944/preprints202401.1733.v1

sagging deformations[6]. This concave sag deformation can intensify the variation in heat flux distribution across the sheet, caused by the altered view factor relative to the heater bank. This might also lead to uneven heat flux on both the upper and lower sides of the sheet, thereby creating temperature gradients both across the surface of the sheet and through its thickness [7]. While increasing the temperature is essential for capturing intricate mould details, it comes with the trade-off of potential sag deformation. To tackle the challenges associated with thermal expansion-induced warpage and sag deformation during heating, a commonly employed technique involves the creation of a pre-forming bubble. This is achieved by applying air pressure within a sealed cabinet to transform the thermoplastic sheet into a bubble-like configuration[8]. Through the generation of a pre-forming bubble, the onset of contact between the positive mould and the material is postponed. This intentional delay allows the material to stretch uniformly, contributing to a more consistent thickness distribution in the final part. Therefore, the creation of a pre-forming bubble serves as a dual-purpose solution, fostering both uniform stretching and controlled contact, ultimately enhancing the overall quality of the thermoforming process. The height of the preforming bubble is a critical parameter in this context, requiring careful matching with the mould height and precise consideration of its location within the forming process. During the subsequent forming stage, the positive mould moves upwards to make contact with the softened thermoplastic sheet. In this phase of thermoforming, the mould and polymer interact at various times and locations, depending on the mould shape, aided by vacuum in between the mould and the sheet to achieve the desired shape. Here the friction between material and mould, which is highly temperature dependent itself [9], exhibits the highest friction load in the region with initial contact [10,11]. This differential in contact timing, combined with the temperature nonuniform distribution field, and material cooling rate across different regions during forming, leads to non-uniform stretching of the polymeric sheet during forming, consequently resulting in an inevitable thickness variation in the final product [1], [12].

In thermoforming, the uniformity of wall thickness, or its distribution, is considered as a key factor in determining the quality of a formed product [13] [14]. To evaluate this aspect of quality during the thermoforming process and to fine-tune the process parameters for industrial applications, in-situ stereo Digital Image Correlation (DIC) as a non-contact method synchronized with a thermal camera, significantly enhances the real-time monitoring of 3D surface large deformations and temperature variations across the entire field in industrial thermoforming applications [15]. This method commonly entails applying a random speckle pattern to the surface of the object and contrasting subsets of images, both 'deformed' and 'undeformed', along with performing camera calibration focused on the region of interest. In experimental setups, a stereo camera system captures these speckled patterns as the sample undergoes deformation. The technique involves correlating images taken from various angles, enabling the tracking of alterations in the 3D surface geometry throughout the deformation process [16]–[18]. Given the substantial nonlinear deformation inherent in vacuum forming processes, it is crucial to employ more than one camera to capture the out-of-plane movements [19], [20]. Seefried and Drummer [21] utilized DIC to investigate the effects of radiation cross-linking and various process parameters. Their research focused on analyzing strain distributions in thermoformed parts, particularly examining how sheet thickness and processing parameters influence these distributions. The implementation of DIC method on an actual vacuum-forming industrial machine, as demonstrated by Van Mieghem et al., [15] was a significant advancement in this field. Their work effectively highlighted the practicality and feasibility of applying stereo DIC in vacuum forming, contributing valuable insights and methodologies to the industry. Building upon this, Van Mieghem et al [22], [23] introduced a methodology for determining wall thickness in thermoformed products in negative vacuum-assisted semi-sphere mould. This method, utilizing in-situ surface strain DIC measurements, effectively validated various strain definition equations, thereby enhancing the precision of thickness calculations in thermoforming processes [22], [23]. Later on, the complexities involved in accurately measuring pressure-induced mechanical strains during bubble-assisted thermoforming of thin gauge thermoplastic sheets were thoroughly examined by Ayadi et al. using DIC techniques [2], [24].

 doi:10.20944/preprints202401.1733.v1

This research aims at an in-depth examination of the thermo-mechanical behavior of heavy gauge ABS thermoplastic sheet in the forming step of the process, from the moment it makes contact with the mould until it fully conforms to a positive semi-sphere mould with 250mm diameter. By synchronizing an integrated approach that combines stereo DIC technology with a thermal imaging camera, The DIC system not only monitors the material's physical deformations but also captures temperature variation, allowing to analyze the material's response to the forming process. Based on this synchronization, the research is designed to precisely map the evolution of strain fields, deformation rates, and real-time temperature variations within the forming process. The main goal of this research is to identify the temperature at which the material undergoes maximum strain and experiences the highest strain rate during the forming process. This investigation will provide the thermo-mechanical range for material characterization, particularly focusing on the material deformation and behavior within the temperature range during the forming stage. The findings from this investigation will play as an instrumental validation case study in enhancing the accuracy of thermoforming simulation. This enhancement involves the development of material characterization test setups that closely mimic the material's behavior under real-world processing conditions [25].

2. Material and Equipment

2.1. Material

In the research, a single-layer ABS EpsoTech AB AN2 V0 extruded material, was used [26]. This type of ABS has a glass transition temperature of 105°C, density of 1.128 g/cm³ and emissivity of 0.8. Figure 1a shows the thermal conductivity of the material as a function of temperature. This property was measured using the C-Therm instrument with Modified Transient Plane Source (MTPS) sensor [27]. The thermal conductivity was measured from 25°C to 140°C, in 10°C intervals, using a convection oven according to the ASTM D7987 standard. The heat capacity of the material as a function of temperature is depicted in Figure 1b. This data was obtained through Differential Scanning Calorimetry (DSC), using a TA Instruments DSC 250. The procedure involved a temperature ramp rate of 20°C/min, with an isothermal hold of 10 minutes both before and after the heating segment. This approach is in accordance to the ASTM E1269 standard, using the three run method. The sample sheet utilized in thermoforming experiment has dimensions of 50 cm by 50 cm, with a nominal thickness of 3mm.

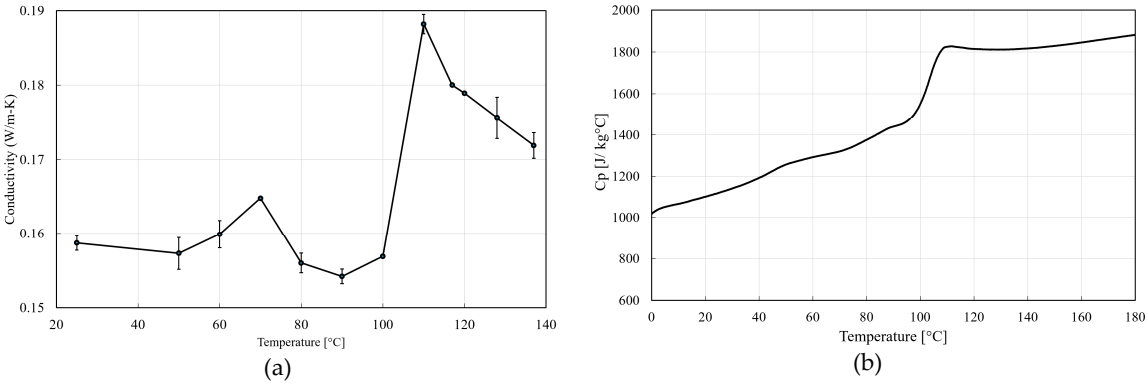

Figure 1. Thermal properties of the ABS EpsoTech material as a function of temperature, **a)** thermal conductivity, **b)** heat capacity.

2.2. Thermoforming Equipment

The thermoforming process was conducted using a GEISS vacuum forming machine, model DU 1000x600x400 U8. This machine is equipped with dual heater banks, positioned above and below of the window plate, each measuring 100 by 60 cm, as shown in Figure 2a. The maximum total electric power of these heater banks is 61.7 kW. Each heater bank is equipped with 54 “Speedium” halogen elements. These elements come in two different coil lengths: 16 cm for 650W elements and 6 cm for

 doi:10.20944/preprints202401.1733.v1

300W elements. The power of each coil is individually adjustable. In this thermoforming machine, the Miniature Infrared (MI) pyrometer sensor by Raytek GmbH is used to measure a surface temperature spot of the thermoplastic sheet while it is being heated. The sensor has an accuracy of ±1%. Based on the optical properties of the material in use, the sensor's emissivity was calibrated to 0.8. Additionally, temperature readings are taken at intervals of every 125 milliseconds. For this experiment, the maximum heating power was considered across the heater banks. The clamping frame was set to 430mm x 430mm. The upper heater bank is positioned at a distance of 180mm from the sheet and the lower heater bank is set at a distance of 153mm (Figure 2b). The clamping frame's height, at 103mm, partially obstructs the radiative heat from effectively reaching the material, especially in the corner areas. A male semi-spherical cast aluminum mould, with a a radius of 125mm, was installed within the machine's sealed cabinet, (Figure 3a). In this experiment, the temperature rise of the mould was monitored using a PT100 RTD temperature sensor. The mould was heated with water to a temperature of 80°C.

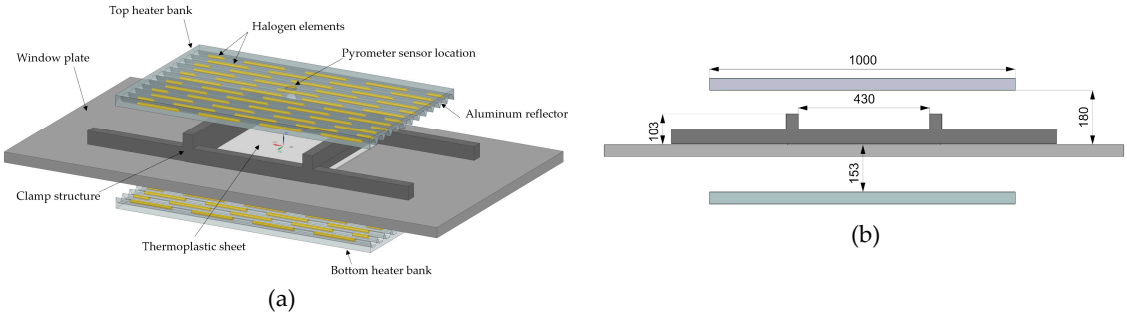

Figure 2. (a) The layout of the GEISS vacuum forming machine DU 1000x600x400 U8, including the positioning of halogen elements, and **(b)** Distance between the upper and lower heater banks in relation to the window plate presented in millimeter.

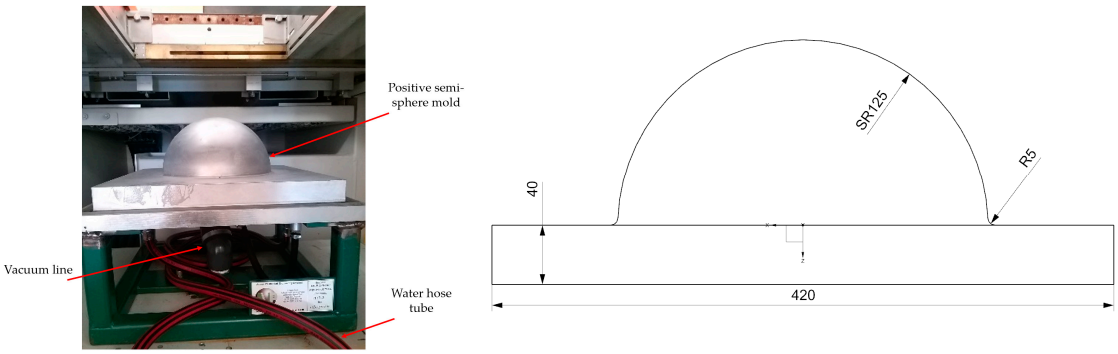

Figure 3. (a) Semi-sphere mould fitted inside the cabinet of the vacuum forming machine, connected to the pressurized circulating water system, and **(b)** the dimensions marked in mm on the aluminum mould.

The design of the thermoforming machine incorporates a programmed delay between the mould's final ascent and the activation of vacuum assistance. For this experiment, a delay duration of 1 second was set. As a result, the material experiences several stages, including initial loading through the mould's upward movement, subsequent reloading via vacuum pressure, and relaxation periods determined by the delay interval. To track the vacuum pressure, a WIKA pressure transducer, capable of measuring between -100 to 300 kPa with a voltage output signal of 0 to 10V and an accuracy of ± 0.5%, was installed in the vacuum line to accurately gauge the vacuum pressure during this phase.

 doi:10.20944/preprints202401.1733.v1

3. Experimental setup

3.1. DIC setup and thermal camera synchronization

DIC was used as a technique for measuring out-of-plane displacement and the rate of deformation during the material forming process in vacuum forming. Figure 4a shows the mounting arrangement of DIC cameras with respect to thermal camera as well as light positioning. A random non-repeatable speckle pattern of consistent size is applied to the material surface using a permanent marker to ensure distinction between pixels (Figure 4b). The complete surface deformation of the material during the forming process is recorded using two high-resolution Blackfly S BFLY-U3-51S5M cameras. These cameras have a resolution of 2080x2444 pixels and are equipped with 5 MP Fujinon HF-12.5SA lenses. The pixel size of these cameras is 3.45µm, feature a sensor size of 8.46mm. In this work, a FLIR thermal camera is utilized, with sensor resolution of 640x480 pixels and a pixel size of 0.017mm. The cameras were mounted on top of the machine at a distance of 83cm using a separate frame structure, to prevent vibrations from the machine during recording, as illustrated in Figure 4a. The cameras were integrated into the MatchID platform using a grabber timing box, shown in Figure 4b [28],[29]. This integration ensured precise synchronization between the DIC and temperature data to effectively track the temporal forming progression throughout the process. Calibration of both the DIC stereo camera and the IR thermal camera requires two distinct steps. For the stereo DIC, a specific calibration plate is utilized [30],[31]. In contrast, the calibration of the IR thermal camera involves using a unique target. This target, characterized by its low thermal expansion coefficient, is coated with paints that have varying emissivity levels and is subjected to controlled heating. The calibration parameters for the stereo DIC system, installed on the GEISS thermo vacuum forming machine, are outlined in Table 1. These parameters are categorized into intrinsic and extrinsic types across three cameras, including two white light cameras (Camera 0 and Camera 1) and one thermal camera (Camera 2). The intrinsic parameters, which are inherent to each camera, include the focal lengths in the x and y directions (f_x, f_y), the coordinates of the camera detector's center (C_x, C_y), and the skewing factor of the sensor array (f_s), along with the first-order lens distortion parameter (κ_1). The extrinsic parameters describe the spatial relationships and orientation between the cameras. The angles (θ, φ, ψ) indicate the rotational alignment between the white light cameras (Camera 0 and Camera 1) and between Camera 0 and the thermal camera (Camera 2). Additionally, the translational distances (T_x, T_y, T_z) quantify the distances between the x, y, and z directions, respectively [32].

Table 1. Calibration parameters of the stereo DIC system mounted on GEISS vacuum forming machine.

Intrinsic parameters	**Camera 0**	**Camera 1**	**Camera 2 (Thermal Camera)**	**Extrinsic parameters**	**DIC white cameras**	**Camera 2 (Thermal Camera)**
f_x [***Pixcel***]	3745	3749	1470	θ (°)	0.32	1.48
f_y [***Pixcel***]	3743	3748	1748	ϕ (°)	-15.09	13.15
C_x [***Pixcel***]	1221	1280	289	Ψ (°)	0.24	0.66
C_y [***Pixcel***]	1050	1062	235	T_x [mm]	180.70	-164.82
f_s [***Pixcel***]	0	-0.95	0.82	T_y [mm]	-1.17	4.05
κ_1	-0.07	-0.08	0.01	T_z [mm]	44.00	56.39

As required for stereo-DIC full field strain measurements, a random speckle pattern of uniform size is applied on half of the sheet surface using a permanent marker with the created average 6.6 pixels in size and exhibit a contrast level of 58.62% as shown in Figure 4c. Only halve of the sheet was examined in this study, due to the symmetric nature of the mould geometry. The continuous correlation during out of plane forming of complex parts is directly linked to the camera orientation relative to the observed surface which changes throughout the forming process [33]. To address this, the cameras were positioned to specifically monitor deformation at the edge of the semi-spherical

 doi:10.20944/preprints202401.1733.v1

mould, a region known to experience maximum stretching during the vacuum process. This positioning is crucial for ensuring continuous correlation, as the material tends to orient in the z-direction when forming into a semi-sphere. It is important to highlight that both cameras must cover the entire area of interest for effective correlation process. Two light sources equipped with polarization filters are used to provide adequate illumination over the region of interest. Throughout the forming process, stereo DIC continuously captures images of the speckled area of interest at a rate of 15 frames per second using MatchID grabber software. These images are then correlated in 3D using the MatchID stereo module, in tandem with synchronized thermal imaging captured via a timing trigger box. The Zero Normalized Sum of Square Difference (ZNSSD) correlation criterion with a subset size of 35 and step size of 3 pixels between two subset was used [34]. In the pair images recording procedures, the subset defines a unique fingerprint which enables the DIC algorithm to detect the position of each subset in the 3D space during material deformation [20], [35]. The strain field is obtained on the speckled pattern surface of the specimen by continuous correlation of the size and the shape of the deformed subset. In the initial phase of the stereo-DIC analysis, the reference state is established using the image pair that captures the onset of contact between the mould and the heated sheet. This approach helps to mitigate the impact of spackle discoloration due to heating, thereby enhancing the correlation in Stereo-DIC analysis. Due to the presence of large deformations each step of correlation is linked to its previous updated state. The strain field was computed using a strain window sized of 15 DIC data points. The correlation settings adopted in MatchID stereo software can be found in Table 2.

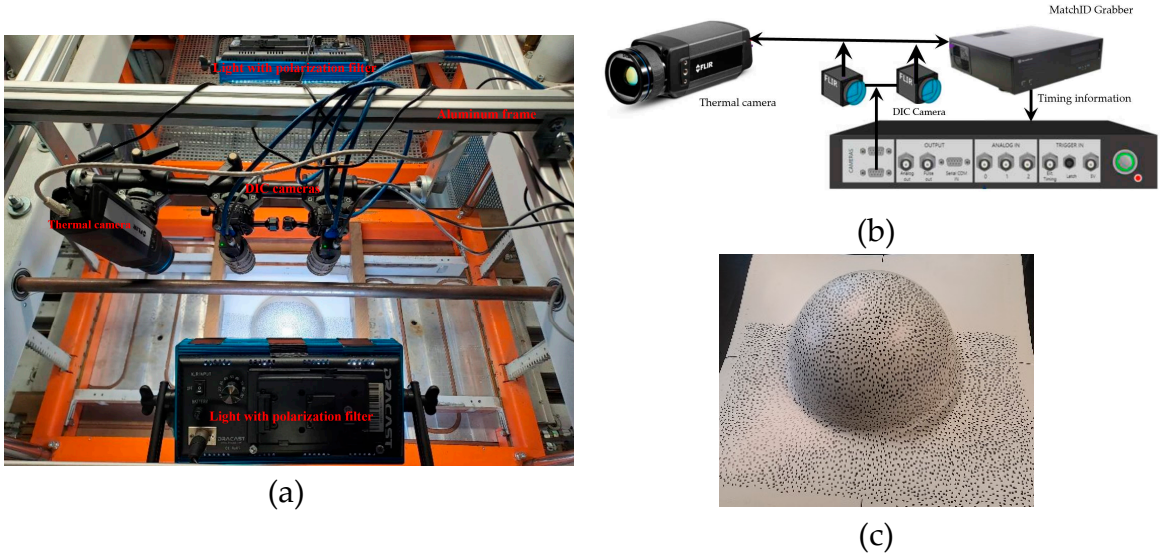

Figure 4. (a) Mounting arrangement of the DIC cameras and thermal camera on the GEISS vacuum forming machine, **(b)** MatchID platform for coupled DIC-thermal camera synchronization, **(c)** Thermoformed product of positive semi-sphere mould of ABS material.

Table 2. Correlation setting using MatchID stereo software.

Parameters	Method
Area of Interest [Pixels]	Polygon shape; 956 x 1560
Correlation algorithm	Zero-normalized sum of squared differences
Interpolation	Local Bicubic Spline Interpolation
Stereo transformation	Affine
Correlation progress	Spatial + update reference
Subset size [Pixels]	35x35
Step size [Pixels]	5
Strain window [Pixels]	15
Strain Shape Function	Polynomial bilinear

 doi:10.20944/preprints202401.1733.v1

Strain tensor	Biot undeformed (Engineering)

3.2. Wall thickness calculation via DIC and validation technique

To quantitatively assess the impact of non-uniform deformation on thickness reduction in different areas, such as the pole and edge of the mould, during the forming process, thickness calculations are performed using the principle of volume conservation [23]. This approach is crucial for determining the stretch ratio in the thickness direction. The stretch ratio for thickness, denoted as λ_3, is derived as the reciprocal of the product of the in-plane stretch ratios in the two principal directions, λ_1 and λ_2. The in-plane stretch ratios are determined by utilizing the engineering strains, represented as ε_1 and ε_2, along their respective principal directions. These strains are extracted using the MatchID stereo software. The formulas defining these relationships are as follows:

$$\lambda_3 = \frac{1}{\lambda_1 \lambda_2} \tag{1}$$

$$\lambda_1 = 1 + \varepsilon_1 \tag{2}$$

$$\lambda_2 = 1 + \varepsilon_2 \tag{3}$$

By integrating these equations, the formula for assessing thickness reduction is given by:

$$t_f = \frac{t_i}{(1+\varepsilon_1)(1+\varepsilon_2)} \tag{4}$$

In this formula, t_f represents the final thickness of the sheet, calculated by taking into account the initial thickness t_i and the engineering strains in the two principal directions.

To verify the accuracy of thickness measurements obtained through the DIC technique, non-destructive testing was conducted on the thermoformed semi-spherical part. This was achieved using an Olympus 38DL PLUS ultrasonic thickness gauge, equipped with an M202 transducer, compatible with thermoplastic material to precisely measure the wall thickness. The M202 transducer operates by sending high-frequency sound waves into the material. When these waves encounter a boundary or interface within the material, they are reflected back to the transducer. The time taken for the sound waves to travel to the boundary and back is measured. Since the speed of sound in the material is known or can be calibrated, this time measurement is used to calculate the thickness of the material. For ABS material, the sound velocity was determined to be 2.32mm/μs. In this measurement, the M202 transducer was operated at a frequency of 10 MHz. The Olympus 38DL PLUS was calibrated using a digital caliper on the same sheet prior to the material's forming process. This step established a standard reference, ensuring the accuracy of subsequent measurements. Additionally, the thickness of the preformed ABS sheet, which was nominally 3mm thick and produced via extrusion, was measured to provide a precise baseline for comparison. Given the nature of the extrusion process, the sheet displayed minor variations in thickness across its surface. To evaluate this variability, measurements were taken at five points: the center and four others, each positioned 10 cm from the center. The results indicated that the maximum deviation in thickness from the center point was reported as 2.91mm with a tolerance of ±0.05mm.

4. Results and Discussion

4.1. Temperature nonuniformity

Figure 5 displays the temperature profile of the sheet through its heating and cooling stages, particularly focusing on the cooling interval before the heated sheet contacts the mould. This data was recorded using the pyrometer sensor located at the center of the top heater bank, as shown in Figure 2a. To implement this experiment the upper heater banks were kept in place but turned off following the heating phase to track the thermoplastic sheet's temperature reduction. Temperature readings were initiated at the beginning of the heating process and were continuously recorded throughout. The data revealed that the target setpoint temperature of 155°C was reached after 33s of

 doi:10.20944/preprints202401.1733.v1

heating. However, a notable temperature drop was observed once the heater bank was deactivated, with the temperature decreasing to 140.3°C within 11s. This time lag corresponds with the typical duration required for the heater bank to retract and the moment when the mould begins its upward movement, making contact with the sheet. It is noted that increasing the mold table speed can effectively minimize the time delay, thus preventing further unwanted drops in temperature. However, this method may risk compromising the material's structural integrity or lead to irregular deformation. Figure 6a shows the temperature distribution across half of the sheet surface at the moment of initial contact. Despite the uniform emitted radiative heat flux from the heater banks, a notable in-plane temperature gradient was observed across the sheet. The temperature distribution, characterized by concentric isothermal lines extending from the center to the edges, revealed that the highest temperature was achieved near the center region. As shown in Figure 6b, the temperature exhibited a steady decline from 140.2°C at the center to 131.5°C towards the edges, indicating a variation of 8.7 degrees. This variation can be primarily attributed to the sizes of the clamping frames, which tend to partially obstruct the transmission of radiative heat to the sheet, particularly in the corner areas.

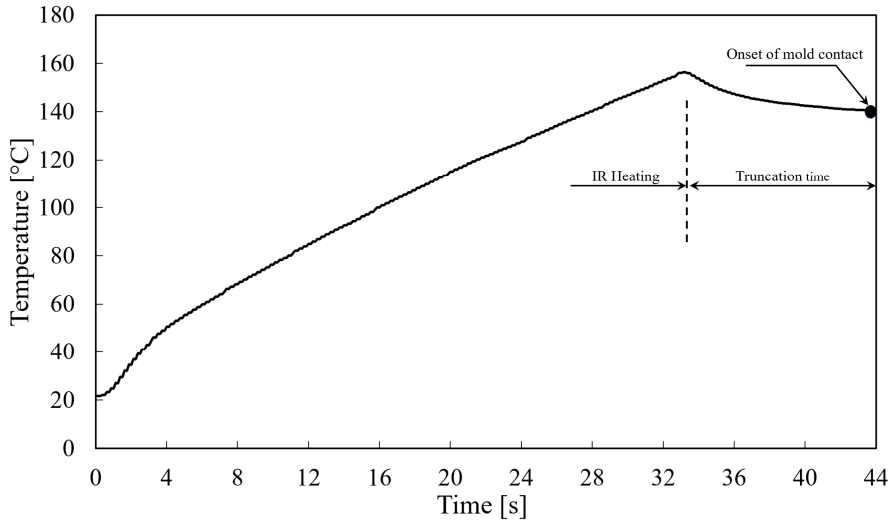

Figure 5. Temperature profile during radiative heating of a nominal 3mm ABS sheet with trigger setpoint of 155°C measured by MI pyrometer sensor followed by cooling at ambient temperature during thermoforming process.

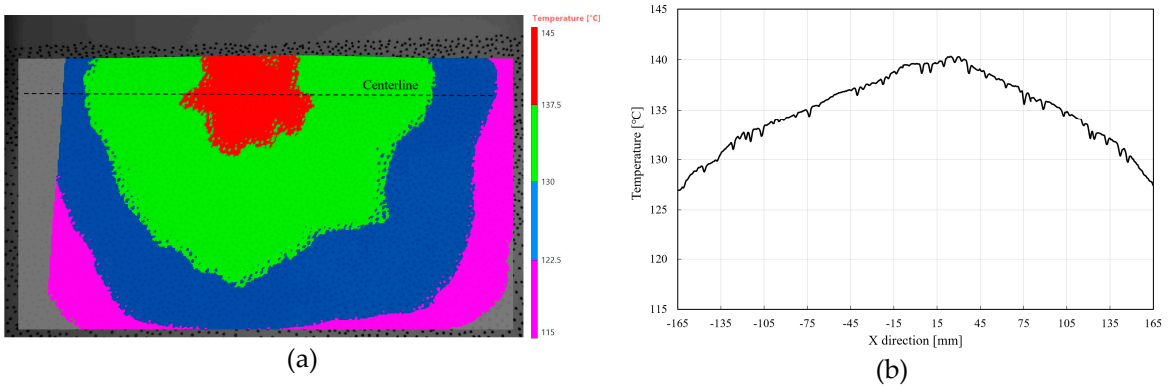

Figure 6. (a) Temperature field across the half of ABS sheet surface just prior forming, **(b)** temperature profile across the centerline.

Conversely, the localized variations in surface flatness, appearing as warpage and sagging from thermal strain, significantly diminished the effectiveness of radiative heating. This reduction in efficiency was mainly due to changes in the view factor, leading to an asymmetrical temperature distribution across the sheet. Additionally, the sagging alters how each part of the sheet interacts with

 doi:10.20944/preprints202401.1733.v1

the heater bank, further disrupting the heat flux distribution. This uneven heating can affect both the top and bottom surfaces of the sheet and result in temperature gradients that complicate the shaping process [7]. The ultimate thickness distribution of the formed part is significantly influenced by the initial temperature distribution within the sheet [36], [37]. Therefore, the intermediate period between the heating stage and the forming process is a critical factor. Increasing the temperature setpoint can lead to more pronounced sag deformation in the sheet. To mitigate this, an effective method is to shorten this time interval, thereby minimizing heat loss through convective heat transfer. This approach entails a quicker movement of the mould, reducing the duration between heating and forming, and thus preserving the desired temperature distribution more effectively.

4.2. Forming of the heated sheet

The forming process starts with the stretching of the heated sheet by the upward movement of the mould. Figure 7 shows the strain field of the forming process. The mould reaches its peak position within 0.73 seconds. The initial contact between the sheet and the top of the mould acts as a constraint, preventing further stretching in the contact area even though it is the warmest part of the sheet. Notably, at the onset of this phase, the sheet displays negligible strain, owing to an existing sag deformation that compensates for the initial mechanical load. Following this, it takes 1s before the vacuum-assisted final forming stage is started. Despite the constancy of the initial strain induced by the mould, the material's internal stress begins to diminish, a characteristic behavior of its viscoelastic nature [38]. Concurrently, the influence of gravity gently continues to stretch the material. Therefore there is a dynamic interaction among mechanical constraints, viscoelastic relaxation, and gravitational forces during this 1s time lag. The sections of the softened sheet that have not yet made contact with the mould predominantly undergo uniaxial stretching, as a result of the vacuum pressure applied. This leads to the material stretching uniaxially around the sphere, beginning from the point of initial contact at the top. The complete shaping process is achieved within a timeframe of 3.8 seconds. Figure 8 indicates the vacuum pressure which progressively increases over time. To examine the impact of vacuum pressure on the forming process, Figure 9 illustrates the engineering strain and strain rate in two distinct regions: the initial contact area located at the pole and the corner side of the semi-sphere mould. These areas are identified as Regions of Interest (ROI) 1 and 2, respectively. During the initial loading, prompted by the mould's upward movement, the maximum strain in ROI 1 is recorded at 5.2%, while in the off-pole region, ROI 2, it reaches 18.3%, (Figure 9a).

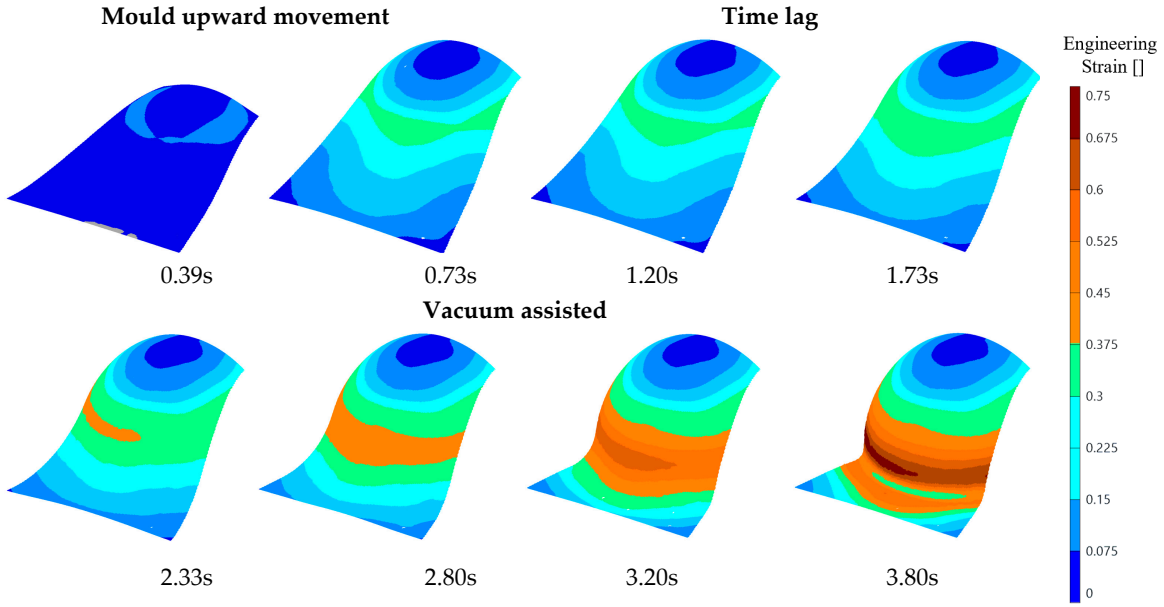

Figure 7. Maximum principal engineering strain of the ABS sheet, recorded at different forming evolution frames through DIC correlation.

 doi:10.20944/preprints202401.1733.v1

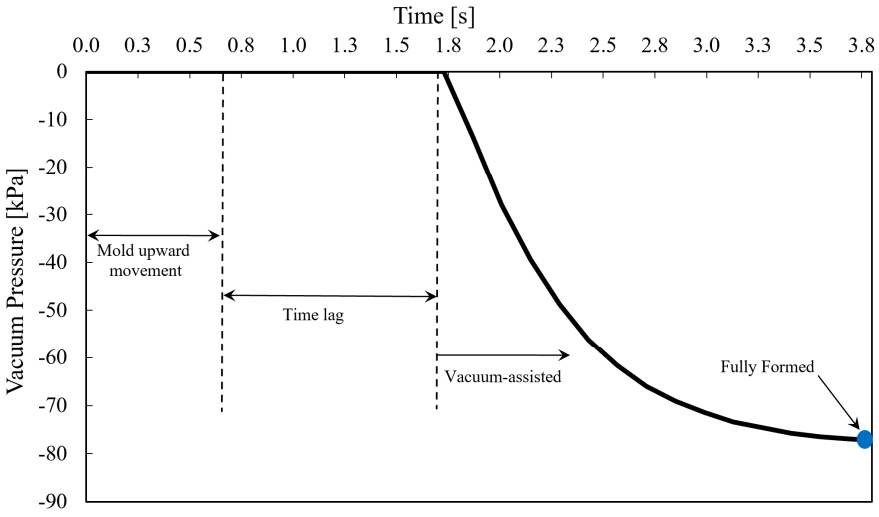

Figure 8. Profile of vacuum pressure spanning from the activation of the vacuum pump to the final stage of material forming.

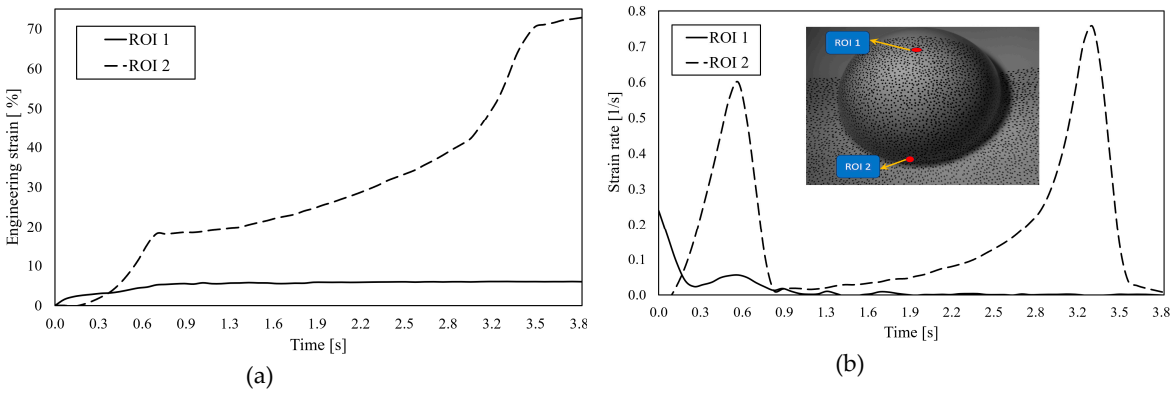

(a) (b)

Figure 9. Diagram depicting **(a)** strain and **(b)** strain rate experienced during the forming of an ABS sheet on a semi-spherical mould. The diagram specifically focuses on two distinct areas: the pole, referred to as Region of Interest 1 (ROI 1), and the edge, labeled as Region of Interest 2 (ROI 2).

The corresponding maximum strain rates for these areas are 0.24 1/s and 0.6 1/s (Figure 9b). In the subsequent 1-second delay, these values experience a slight increase to 5.6% and 21.1% for ROI 1 and ROI 2, respectively. Although these measurements indicate an uneven distribution of strain, introducing bubble formation at this stage could effectively improve strain field uniformity. This can be achieved by delaying the mould's contact with the heated sheet. The successful implementation of this technique relies on carefully balancing several critical parameters: the mould's shape, the distribution of temperature, the timing, and the height of bubble formation.

During the vacuum-assisted pressure moulding process, significant stretching is observed in areas that are not in immediate contact with the mould. This is particularly evident in ROI 2, which experiences considerable straining. The strain in this area reaches up to 72.8%, accompanied by a peak strain rate of 0.76 1/s. From this observation, it can be inferred that once the material makes contact with the mould, further stretching is minimal, regardless of the applied temperature.

Consequently, the points of the material that contact the mould last tend to undergo the most stretching, as there is limited material remaining to conform to the mould's surface. Figure 10 is pivotal in pinpointing the surface temperature at which the most significant deformation takes place during the forming process. This figure follows the shifts in temperature from the moment the sheet first touches the mould to the completion of its shaping. It vividly captures the sheet's gradual cooling while in contact with the mould, effectively illustrating the material's response and transformation under various thermal conditions throughout the moulding sequence.

 doi:10.20944/preprints202401.1733.v1

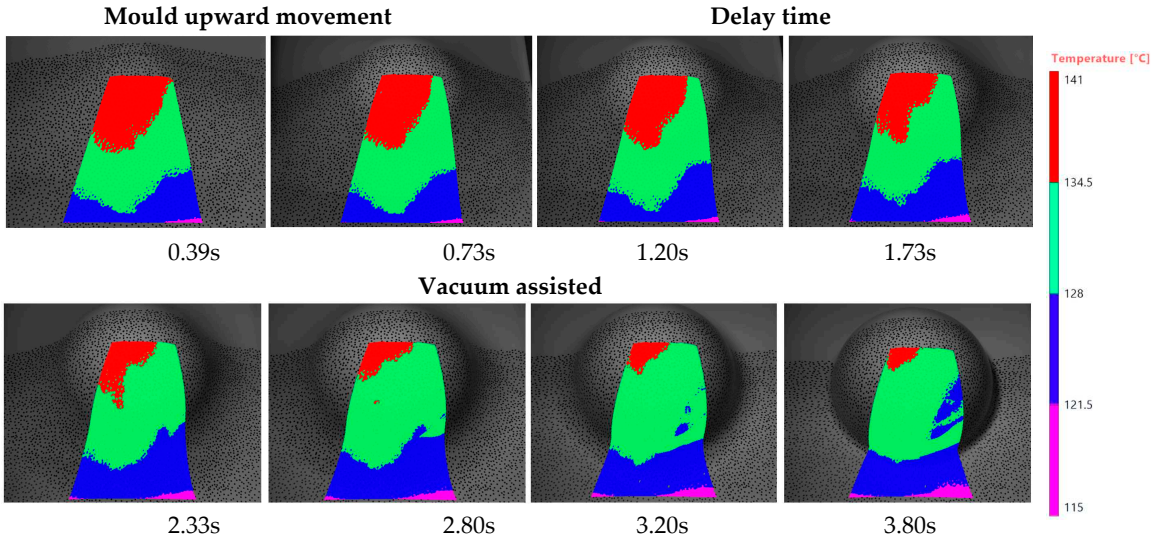

Figure 10. Temperature field during the forming process of a heated ABS sheet on a semi-spherical mould, ranging from the initial contact of the sheet with the mould to the completion of the forming process.

Figure 11 provides a detailed view of the temperature variations in the pole region (ROI 1) and the edge region (ROI 2) during the forming process. ROI 1, making initial contact with the mould at 80°C, shows a notable decrease in surface temperature, dropping by 6°C. Figure 12 effectively captures the evolution of thickness during the forming process. It highlights that the region first in contact with the mould during the initial loading phase undergoes minimal stretching in the later vacuum pressure phase.

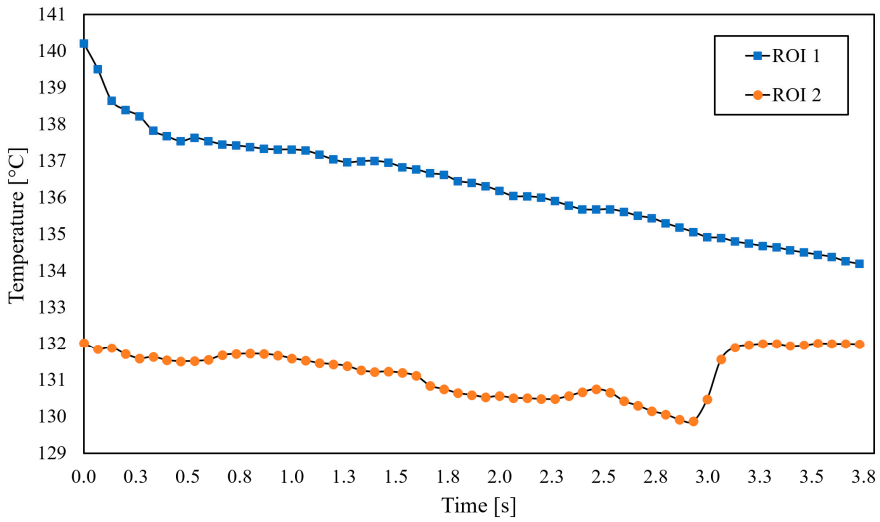

Figure 11. Temperature Variations at pole Region (ROI 1)and edge region (ROI 2) during thermo-vacuum forming process of an ABS Sheet.

In contrast, ROI 2, which undergoes the most deformation, exhibits stable temperature, consistently around 131 ± 1°C throughout the entire process. As the vacuum pressure is applied, the material increasingly conforms to the mould surface, stretching further until it adheres to the mould, with no additional thickness reduction observed.

The area near the corner, being the last to contact the mould, experiences the most pronounced thickness reduction, reaching a minimum of 1.94mm, as detailed in Figure 13. To validate the thickness measurements obtained through DIC technique, wall thickness was also measured at every centimeter along the y-axis arc length using an ultrasonic thickness gauge. The results closely align

 doi:10.20944/preprints202401.1733.v1

with the DIC-derived values, thereby confirming the accuracy and reliability of the full-field strain measurements recorded during the test.

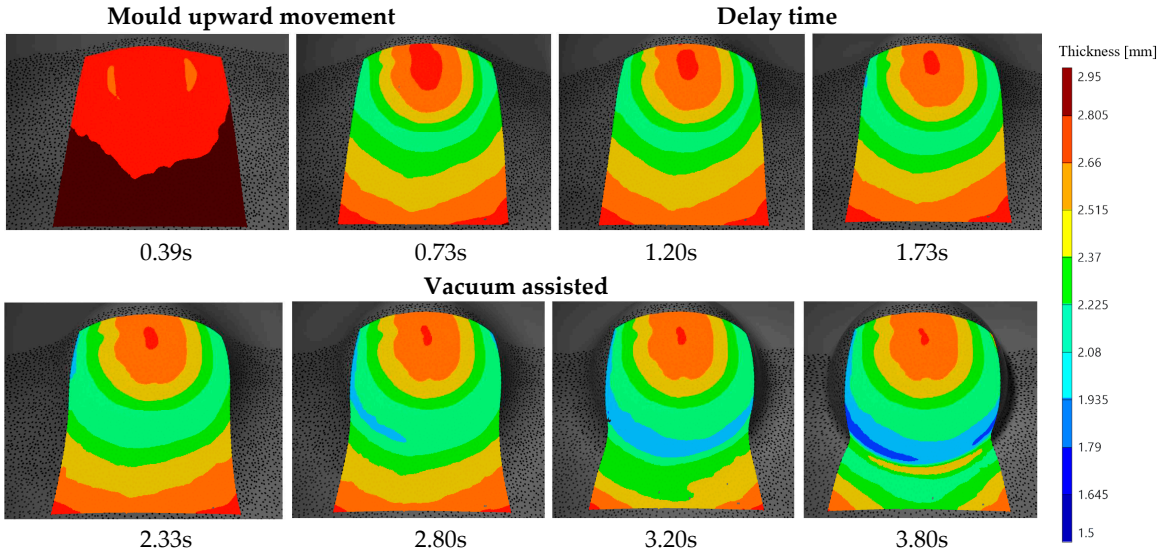

Figure 12. Thickness distribution in 3mm nominal thickness ABS sheet during vacuum-assisted thermoforming on a semi-spherical positive Mould.

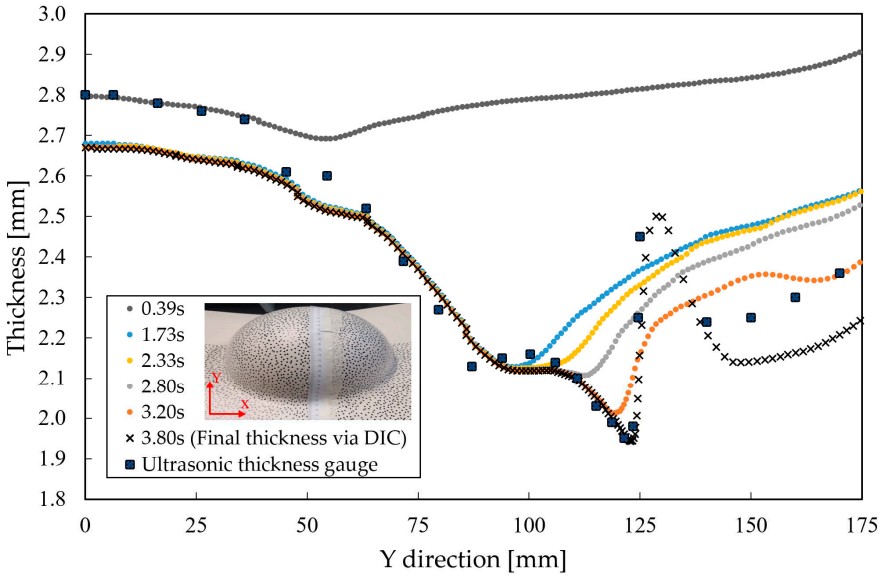

Figure 13. Evolution of thickness reduction in an ABS sheet during forming calculated using Digital Image Correlation (DIC) method, with comparative data from an ultrasonic thickness across Y axis.

5. Conclusions

This study provides an in-depth analysis of the thermo-mechanical properties of heavy gauge ABS thermoplastic during the positive vacuum thermoforming process, with a particular focus on the forming stage where the material interacts with the mould. Utilizing Digital Image Correlation (DIC) in tandem with thermal imaging, the research effectively mapped the correlation between real-time strain fields, deformation rates, and temperature fluctuations on the thermoplastic sheet during vacuum forming. Experiment validation was achieved by comparing thickness calculations obtained from DIC's principal strain directions to directly measured thickness values using ultrasonic testing. This confirms the accuracy of the full-field strain measurements. While the cut-off temperature for the heaters was 155°C, the study revealed that due to the processing settings, the maximum strain occurs at a notably lower temperature of 131°C. Addressing this discrepancy with heat patterns from

heater elements is problematic for small moulds due to the size compatibility issues between the heater elements and the mould. This situation highlights the significant role of time delay between heating and forming, which results in unwanted temperature drops. A proposed solution is to accelerate the mould table's movement, potentially reducing the time gap and increasing the strain on the heated sheet. However, this approach could compromise the material's structural integrity or cause irregular deformation. An alternative solution is to construct a temperature-regulated enclosure around the forming area. This would help sustain a steady temperature, minimizing heat loss, and thus improving the process's effectiveness. The outcomes of this experiment offers potential applicability as a benchmark case study for the validation of simulation packages specifically designed for thermoforming simulations.

Author Contributions: Conceptualization, R.V., B.B., and F.D.; methodology, R.V., B.B., and F.D.; investigation, R.V; resources, F.D.; writing—original draft preparation, R.V.; writing—review and editing, B.B., and F.D.; visualization, R.V. and B.B.; supervision, F.D.; funding acquisition, B.B. and F.D. All authors have read and agreed to the published version of the manuscript.

Funding: This work has been funded by the ICON project "ProPeL", which fits in the MacroModelMat (M3) research program, coordinated by Siemens (Siemens Digital Industries Software, Belgium), and funded by SIM (Strategic Initiative Materials in Flanders) and VLAIO (Flemish government agency Flanders Innovation & Entrepreneurship). The authors would like to express their profound gratitude to Dr. Güven Ogus and Dr. Pascal Lava of the MatchID team for their invaluable assistance and support. Special thanks are also due to the Vitalo Group company for kindly supplying the ABS sheet materials in a range of thicknesses and dimensions.

Data Availability Statement: Data will be made available on request.

Conflicts of Interest: The authors declare no conflict of interest.

References

1. A. Ayadi, M. F. Lacrampe, and P. Krawczak, "A comprehensive study of bubble inflation in vacuum-assisted thermoforming based on whole-field strain measurements," *AIP Conf. Proc.*, vol. 1960, no. December, 2018, doi: 10.1063/1.5034972.
2. A. Ayadi, M. F. Lacrampe, and P. Krawczak, "Bubble assisted vacuum thermoforming: considerations to extend the use of in-situ stereo-DIC measurements to stretching of sagged thermoplastic sheets," *Int. J. Mater. Form.*, vol. 13, no. 1, pp. 59–76, 2020, doi: 10.1007/s12289-018-01467-y.
3. F. M. Duarte and J. A. Covas, "IR sheet heating in roll fed thermoforming: Part 1 - Solving direct and inverse heating problems," *Plast. Rubber Compos.*, vol. 31, no. 7, pp. 307–317, 2002, doi: 10.1179/146580102225006530.
4. Y. Li and J. A. Nemes, "Membrane Inflation of Polymeric Materials: Experiments and Finite Element Simulations," *Polym. Eng. Sci.*, vol. 41, no. 8, pp. 1399–1412, 2001.
5. J. L. Throne, "The effect of sheet sag on radiant energy transmission in thermoforming," *Thermoforming Q.*, vol. 25, no. 4, pp. 19–24, 2006.
6. A. M. Jordan, L. Meyer, K. Kim, B. Lee, F. S. Bates, and C. W. Macosko, "Improved Polypropylene Thermoformability through Polyethylene Layering," *ACS Appl. Mater. Interfaces*, 2021, doi: 10.1021/acsami.2c08586.
7. A. J. Giacomin, A. W. Mix, and O. Mahmood, "Sag in thermoforming," *Polym. Eng. Sci.*, vol. 50, no. 10, pp. 2060–2068, 2010, doi: 10.1002/pen.21734.
8. E. Verron, G. Marckmann, and B. Peseux, "Dynamic inflation of non-linear elastic and viscoelastic rubber-like membranes," *Int. J. Numer. Methods Eng.*, vol. 50, no. 5, pp. 1233–1251, 2001, doi: 10.1002/1097-0207(20010220)50:5<1233::AID-NME77>3.0.CO;2-W.
9. J. K. Lee, T. L. Virkler, and C. E. Scott, "Effects of rheological properties and processing parameters on ABS thermoforming," *Polym. Eng. Sci.*, vol. 41, no. 2 SPEC. ISS, pp. 240–261, 2001, doi: 10.1002/pen.10725.
10. M. K. Warby, J. R. Whiteman, W. G. Jiang, P. Warwick, and T. Wright, "Finite element simulation of thermoforming processes for polymer sheets," *Math. Comput. Simul.*, vol. 61, no. 3–6, pp. 209–218, 2003, doi: 10.1016/S0378-4754(02)00077-0.
11. R. A. Morales, M. V. Candal, O. O. Santana, A. Gordillo, and R. Salazar, "Effect of the thermoforming process variables on the sheet friction coefficient," *Mater. Des.*, vol. 53, pp. 1097–1103, 2014, doi: 10.1016/j.matdes.2013.08.009.
12. M. Takaffoli, G. Hangalur, R. Bakker, and N. Chandrashekar, "Thermo-visco-hyperelastic behavior of polycarbonate in forming of a complex geometry," *J. Manuf. Process.*, vol. 57, no. June, pp. 105–113, 2020, doi: 10.1016/j.jmapro.2020.06.019.

13. W. de O. Leite, J. C. C. Rubio, F. M. Cabrera, A. Carrasco, and I. Hanafi, "Vacuum thermoforming process: An approach to modeling and optimization using artificial neural networks," *Polymers (Basel).*, vol. 10, no. 2, 2018, doi: 10.3390/polym10020143.
14. J. Throne, *16 Thermoforming*. 2017.
15. B. Van Mieghem, F. Desplentere, A. Van Bael, and J. Ivens, "Improvements in thermoforming simulation by use of 3D digital image correlation," *Express Polym. Lett.*, vol. 9, no. 2, pp. 119–128, 2015, doi: 10.3144/expresspolymlett.2015.13.
16. M. A. Sutton, J. H. Yan, V. Tiwari, H. W. Schreier, and J. J. Orteu, "The effect of out-of-plane motion on 2D and 3D digital image correlation measurements," *Opt. Lasers Eng.*, vol. 46, no. 10, pp. 746–757, 2008, doi: 10.1016/j.optlaseng.2008.05.005.
17. X. Shao, X. Dai, Z. Chen, Y. Dai, S. Dong, and X. He, "Calibration of stereo-digital image correlation for deformation measurement of large engineering components," *Meas. Sci. Technol.*, vol. 27, no. 12, 2016, doi: 10.1088/0957-0233/27/12/125010.
18. F. Hild and S. Roux, "Digital image correlation: From displacement measurement to identification of elastic properties - A review," *Strain*, vol. 42, no. 2, pp. 69–80, 2006, doi: 10.1111/j.1475-1305.2006.00258.x.
19. X. D. Ke, H. W. Schreier, M. A. Sutton, and Y. Q. Wang, "Error Assessment in Stereo-based Deformation Measurements," *Exp. Mech.*, vol. 51, no. 4, pp. 423–441, 2011, doi: 10.1007/s11340-010-9450-3.
20. M. Jerabek, Z. Major, and R. W. Lang, "Strain determination of polymeric materials using digital image correlation," *Polym. Test.*, vol. 29, no. 3, pp. 407–416, 2010, doi: 10.1016/j.polymertesting.2010.01.005.
21. A. Seefried and D. Drummer, "The effects of radiation cross-linking and process parameters on the behavior of polyamide 12 in vacuum thermoforming," *Polym. Eng. Sci.*, vol. 52, no. 4, pp. 884–892, 2012, doi: 10.1002/pen.22155.
22. B. Van Mieghem, J. Ivens, and A. Van Bael, "Consistency of Strain Fields and Thickness Distributions in Thermoforming Experiments Through Stereo DIC," *Exp. Tech.*, vol. 40, no. 5, pp. 1409–1420, 2016, doi: 10.1007/s40799-016-0143-4.
23. B. Van Mieghem, P. Lava, D. Debruyne, A. Van Bael, and J. Ivens, "Digital image correlation for on-line wall thickness measurements in thick gauge thermoforming," *Key Eng. Mater.*, vol. 554–557, pp. 1583–1591, 2013, doi: 10.4028/www.scientific.net/KEM.554-557.1583.
24. A. Ayadi, M. F. Lacrampe, and P. Krawczak, "Assessment of principal strain uncertainties in stereo-DIC due to uncontrollable change of initial boundary conditions during vacuum-assisted thermoforming," *AIP Conf. Proc.*, vol. 2113, no. July, 2019, doi: 10.1063/1.5112662.
25. R. Varedi, B. Buffel, and F. Desplentere, "Characterization of the biaxial response of a thermoplastic ABS Sheet using DIC-instrumented bubble inflation technique," *Mater. Res. Proc.*, vol. 28, pp. 1887–1896, 2023, doi: 10.21741/9781644902479-204.
26. "epsotech Holding GmbH, Technical datasheet for epsotech AB AN2 V0," 2019. [Online]. Available: https://epsotech.com/files/uploads/epsotech/2020/AB AN2 V0.pdf.
27. M. Mokarizadehhaghighishirazi, B. Buffel, S. V. Lomov, and F. Desplentere, "Homogenisation of the Local Thermal Conductivity in Injection-Moulded Short Fibre Reinforced Composites," *Polymers (Basel).*, vol. 14, no. 16, 2022, doi: 10.3390/polym14163360.
28. "MatchID." http://www.matchid.eu/ (accessed May 22, 2019).
29. P. Lava, S. Cooreman, S. Coppieters, M. De Strycker, and D. Debruyne, "Assessment of measuring errors in DIC using deformation fields generated by plastic FEA," *Opt. Lasers Eng.*, vol. 47, no. 7–8, pp. 747–753, 2009, doi: 10.1016/j.optlaseng.2009.03.007.
30. E. Fauster, P. Schalk, and P. L. O'Leary, "Evaluation and calibration methods for the application of a video-extensometer to tensile testing of polymer materials," *Mach. Vis. Appl. Ind. Insp. XIII*, vol. 5679, no. 0, p. 187, 2005, doi: 10.1117/12.586734.
31. Z. Wang, H. Kieu, H. Nguyen, and M. Le, "Digital image correlation in experimental mechanics and image registration in computer vision: Similarities, differences and complements," *Opt. Lasers Eng.*, vol. 65, pp. 18–27, 2015, doi: 10.1016/j.optlaseng.2014.04.002.
32. P. Lava, E. M. C. Jones, L. Wittevrongel, and F. Pierron, "Validation of finite-element models using full-field experimental data: Levelling finite-element analysis data through a digital image correlation engine," *Strain*, vol. 56, no. 4, pp. 1–17, 2020, doi: 10.1111/str.12350.
33. E. Parsons, M. C. Boyce, and D. M. Parks, "An experimental investigation of the large-strain tensile behavior of neat and rubber-toughened polycarbonate," *Polymer (Guildf).*, vol. 45, no. 8, pp. 2665–2684, 2004, doi: 10.1016/j.polymer.2004.01.068.
34. S. Yaofeng and J. H. L. Pang, "Study of optimal subset size in digital image correlation of speckle pattern images," *Opt. Lasers Eng.*, vol. 45, no. 9, pp. 967–974, 2007, doi: 10.1016/j.optlaseng.2007.01.012.
35. H. W. Schreier and M. A. Sutton, "Systematic errors in digital image correlation due to undermatched subset shape functions," *Exp. Mech.*, vol. 42, no. 3, pp. 303–310, 2002, doi: 10.1177/001448502321548391.

36. F. M. Schmidt, Y. Le Maoult, and S. Monteix, "Modelling of infrared heating of thermoplastic sheet used in thermoforming process," *J. Mater. Process. Technol.*, vol. 143–144, no. 1, pp. 225–231, 2003, doi: 10.1016/S0924-0136(03)00291-7.
37. B. Buffel, B. Van Mieghem, A. Van Bael, and F. Desplentere, "Optimization of the IR-heating phase in thermoforming of thermoplastic sheets: Characterization and modelling," *AIP Conf. Proc.*, vol. 1914, no. December 2017, 2017, doi: 10.1063/1.5016687.
38. J. S. Bergström and M. C. Boyce, "Constitutive modeling of the large strain time-dependent behavior of elastomers," *J. Mech. Phys. Solids*, vol. 46, no. 5, pp. 931–954, 1998, doi: 10.1016/S0022-5096(97)00075-6.